



**HAL**  
open science

## Shearing interferometry via geometric phase

Luis A Alemán-Castaneda, Bruno Piccirillo, Enrico Santamato, Lorenzo Marrucci, Miguel Alonso

► **To cite this version:**

Luis A Alemán-Castaneda, Bruno Piccirillo, Enrico Santamato, Lorenzo Marrucci, Miguel Alonso. Shearing interferometry via geometric phase. *Optica*, 2019, 6 (4), pp.396. 10.1364/OP-TICA.6.000396 . hal-02072174

**HAL Id: hal-02072174**

**<https://hal.science/hal-02072174>**

Submitted on 19 Mar 2019

**HAL** is a multi-disciplinary open access archive for the deposit and dissemination of scientific research documents, whether they are published or not. The documents may come from teaching and research institutions in France or abroad, or from public or private research centers.

L'archive ouverte pluridisciplinaire **HAL**, est destinée au dépôt et à la diffusion de documents scientifiques de niveau recherche, publiés ou non, émanant des établissements d'enseignement et de recherche français ou étrangers, des laboratoires publics ou privés.

# Shearing interferometry via geometric phase

LUIS A. ALEMÁN-CASTANEDA<sup>1</sup>, BRUNO PICCIRILLO<sup>2,\*</sup>, ENRICO SANTAMATO<sup>2</sup>,  
LORENZO MARRUCCI<sup>2,3</sup>, AND MIGUEL A. ALONSO<sup>1,4,5</sup>

<sup>1</sup>The Institute of Optics, University of Rochester, Rochester NY 14627, USA

<sup>2</sup>Dipartimento di Fisica "Ettore" Pancini, Università di Napoli Federico II, Complesso Universitario MSA, Napoli, Italy

<sup>3</sup>CNR-ISASI, Institute of Applied Science and Intelligent Systems, Via Campi Flegrei 34, Pozzuoli (NA), Italy

<sup>4</sup>Center for Coherence and Quantum Optics, University of Rochester, Rochester NY 14627, USA

<sup>5</sup>Aix-Marseille Univ., CNRS, Centrale Marseille, Institut Fresnel, UMR 7249, 13397 Marseille Cedex 20, France

\*Corresponding author: [bruno.piccirillo@unina.it](mailto:bruno.piccirillo@unina.it)

Compiled March 19, 2019

**We propose an approach based on geometric phase for performing several types of shearing interferometry through a robust, compact, common-path setup. The key elements are two identical parallel plates with spatially-varying birefringence distributions, which perform the shearing by writing opposite geometric phases on the two circular polarization components of the linearly polarized incident wavefront. This setup allows the independent control of the shearing magnitude and relative phase of the two wavefront replicas. The approach is first illustrated for the simplest case of lateral shearing, and then extended to other geometries where the magnitude and direction of the shear vary smoothly over the wavefront.**

<http://dx.doi.org/10.1364/optica.XX.XXXXXX>

*Introduction* – Shearing interferometry is a widespread technique for analyzing optical wavefronts. Its main feature is that of not requiring a known reference; instead, two replicas of the test wavefront are made to interfere after being displaced laterally (lateral shearing), resized differently (radial shearing), or mutually rotated (azimuthal shearing) [1, 2]. The interferogram's interpretation depends not only on the type of shearing but also on its amount – the shear distance (SD) –, and the relative phase difference between the replicas – the shear phase (SP). In typical common-path layouts based on Snell refraction/reflection, such as shear plates or more complex setups [3–5], the SD and SP are coupled and depend on the position or orientation of an optical element. Several mechanisms have been suggested to control SD and SP independently [1, 6–9]. In particular, polarization-based shearing naturally presents this feature because the two replicas are orthogonally polarized. However, polarization-based shearing interferometers often require several optical components and tend to be bulky or expensive [10–14]. More recent propos-

als include the Quadriwave lateral shearing interferometer, a compact diffraction-based device that allows the simultaneous retrieval of two orthogonal directional derivatives [15–18].

In this work, we propose a novel and flexible mechanism for implementing shearing interferometry, based on geometric phase [19, 20]. This mechanism allows for a compact, common-path simple setup for which the SD and SP can be varied continuously and independently. The wavefront under test is separated into two orthogonally-polarized replicas that are mutually displaced through an appropriate sequence of geometric and dynamic phase transformations. The geometric phase is introduced via devices referred to as Spatially Varying Axis birefringent Plates (SVAPs) [21–23]. We begin with the simplest case of lateral shearing, and then discuss the flexibility of this approach for implementing many types of shearing, including radial.

*Methods* – A SVAP is a half-wave retardation plate whose fast-axis direction  $\Theta(x, y)$  varies spatially. After passing through it, a circularly-polarized input beam acquires a *geometric phase factor*  $e^{\pm i2\Theta(x, y)}$ , where the sign depends on the incident polarization handedness  $C_{\pm} = (x \pm iy) / \sqrt{2}$ , which is reversed by the SVAP. The geometric-phase shearing interferometer (GPSI) is based on two identical SVAPs separated by a distance  $\zeta$ .

The bottom-right inset in Fig. 1 shows the fast-axis distribution for the SVAP fabricated for lateral shearing – referred to here as a  $\Lambda$ -plate – superimposed to its near-field white-light image between crossed polarizers. For this device, the fast axis rotates in the transverse plane along the  $x$  direction, the rotation angle  $\Theta$  increasing (or decreasing) linearly with  $x$  from 0 to  $\pi$  over a distance  $\Lambda$ , representing the spatial period of the plate. A  $\Lambda$ -plate then deflects light with circular polarization  $C_{\pm}$  by an angle  $\pm \arctan(\lambda / \Lambda)$ , where  $\lambda$  is the wavelength (Fig. 1). At a distance  $z$  from the plate, such deflection causes a lateral shear  $\pm z\lambda / \Lambda$  from the incident propagation direction.

Consider now an incident linearly-polarized beam:

$$E(x, y, 0) = E(x, y, 0)x = \frac{1}{\sqrt{2}}E(x, y, 0)(C_+ + C_-). \quad (1)$$

After crossing the  $\Lambda$ -plate and propagating in free space, this beam splits into two equally intense circularly-polarized beams,

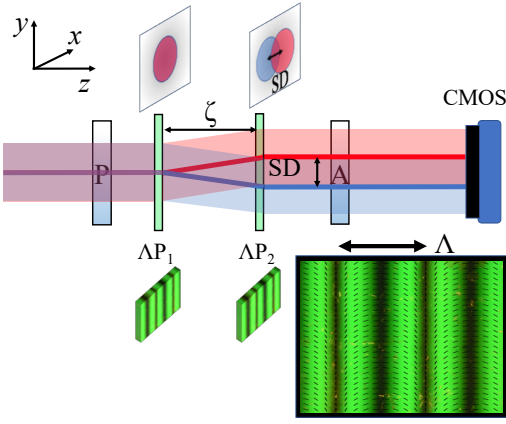


**Fig. 1.** Sketch of a GPSI. The linearly polarized light leaving the polarizer  $P$  can be described as the sum of two identical wavefronts with opposite circular polarizations. Two identical  $\Lambda$ -plates with separation  $\zeta$  introduce a controlled shear between wavefront replicas, and an analyzer  $A$  selects the polarization component used for studying their interference. The bottom-right inset shows the fast-axis distribution of the  $\Lambda$ -plates we fabricated, superposed to their experimental fringe pattern. The spatial period  $\Lambda = (1.32 \pm 0.01)$  mm corresponds to a fast-axis rotation of  $\pi$ .

which are displaced, tilted replicas of the input beam:

$$E_{\pm}(x, y, z) = \frac{1}{\sqrt{2}} E \left( x \mp \frac{\lambda z}{\Lambda}, y, z \right) \exp \left( \pm i \frac{2\pi}{\Lambda} x \right) C_{\pm}, \quad (2)$$

where a common propagation phase is omitted. These replicas are mutually sheared in  $x$  by  $SD(z) = 2z\lambda/\Lambda$ . A second  $\Lambda$ -plate at  $z = \zeta$  reverses again the replicas' polarization handedness, and deflects them back towards the original direction, fixing their shear distance to  $SD = 2\zeta\lambda/\Lambda$  for  $z \geq \zeta$ . That is, varying the  $\Lambda$ -plate separation  $\zeta$  allows accurate control of the  $SD$ . The pair of  $\Lambda$ -plates then behaves like a Savart plate of controllable thickness, but with circular eigenpolarizations rather than linear.

In order to make the replicas interfere, an output linear analyzer is used. The intensity at a detector following the analyzer depends on the angular mismatch  $\psi$  between the input linear polarization direction and the axis of the analyzer, according to

$$I(\psi) \propto |E_+ e^{i\psi} + E_- e^{-i\psi}|^2 = |S|^2 \cos^2 \psi + |D|^2 \sin^2 \psi + \text{Im}(SD^*) \sin 2\psi, \quad (3)$$

where  $S = E_+ + E_-$ ,  $D = E_+ - E_-$  and  $*$  denotes complex conjugation. (Note that, for small  $SD$ ,  $|S| \gg |D|$ .) That is,  $SP = 2\psi$  can be controlled by rotating either the input polarization direction or the output analyzer. By setting  $\psi = 0$ , for example, the GPSI's output is the intensity of  $S$ , which for small  $SD$  is very similar to the intensity of the input beam and provides no significant new information. On the other hand, for  $\psi = \pi/2$ , the GPSI operates in differential mode (henceforth referred to as DM operation) and the output is the intensity of the difference  $D$  between the replicas. Note that in DM operation, if  $SD \ll w$ , where  $w$  denotes the characteristic length of the field transverse profile, from Eq. (3),  $I(\pi/2)$  is approximately proportional to the squared modulus of the  $x$ -derivative of the optical field in the detector plane (otherwise, it returns a fringe pattern). To access the sign of the derivative, one can slightly shift the angle  $\psi$  away

from  $\pi/2$  such that the first and third terms in Eq. (3) become the leading contributions and have similar peak values. Notice that a similar strategy is used in differential image contrast (DIC) microscopy [24, 25] as well as in weak measurements [26].

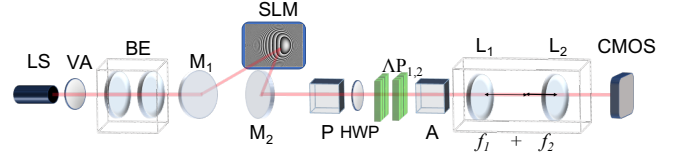


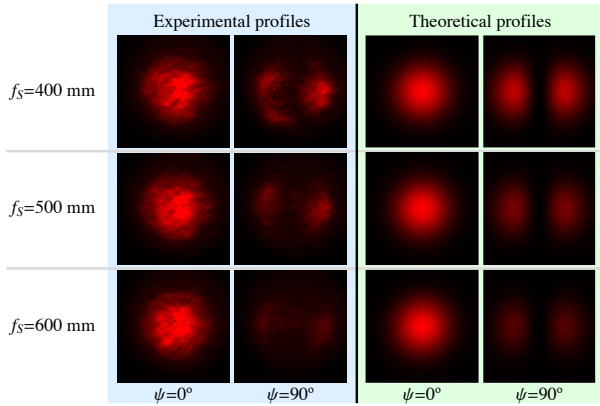
**Fig. 2.** Sketch of the experimental apparatus. (a) A He-Ne laser beam passes through a variable attenuator (VA) and is expanded with a telescope (BE,  $3 \times$  Mag). Two metallic mirrors ( $M_1$  and  $M_2$ ), placed on flip mounts, enable including/excluding a spatial light modulator (SLM) for generating test wavefronts holographically. When  $M_1$  and  $M_2$  are down, optical components can be inserted into the apparatus and analyzed. The half-wave plate HWP is used to rotate the input linear polarization with respect to the axis of the analyzer  $A$ . A telescope is used to image onto the CMOS camera the test beam's transverse cross-section. The lenses  $L_1$  and  $L_2$  have focal lengths  $f_1 = 500$  mm and  $f_2 = 100$  mm respectively.

*Experimental implementation* – The setup is shown in Fig. 2 and described in its caption. The  $\Lambda$ -plates we fabricated consist of a nematic liquid crystal film with nominal thickness  $L = 6 \mu\text{m}$ , sandwiched between two glass substrates coated with an azodye-based photoaligning material suited for molecule orientational anchoring. As shown in the inset in Fig. 1, a real  $\Lambda$ -plate imparts a geometric phase change that is only approximately linear: there is a small deviation from linearity that causes a change of the order of  $10^{-2}$  for the field amplitude, which is below the SNR of the interferometer.

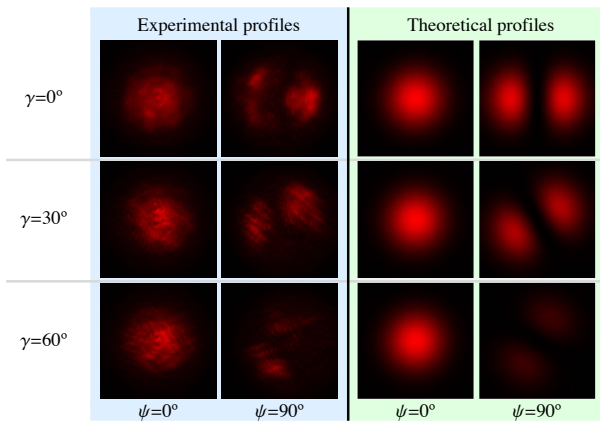
The  $\Lambda$ -plate's retardation is uniform and can be fine-tuned to a half wave for any wavelength by applying an external AC voltage (with RMS of the order of a few volts and frequency of about 10 kHz). This fine-tunability is important in DM operation given the small SNR. Further, the ability to electrically switch the phase retardation between  $\pi$  and 0 enables turning on and off the lateral shear without misalignment. The plates' period is  $\Lambda = (1.36 \pm 0.01)$  mm. By using a linearly polarized He-Ne laser ( $\lambda = 632.8$  nm,  $P_{out} = 5$  mW), we found that a change of 1 mm in the plate separation  $\zeta$  leads to a change of  $1 \mu\text{m}$  in  $SD$ . The minimum plate separation is  $\zeta_{min} = 4$  mm due to the plate mounting. The waist of the illuminating Gaussian beam was expanded to 1.5 mm, effectively behaving as a plane wave over an  $SD$  range of several tens of  $\mu\text{m}$ . Test wavefronts were generated with a liquid-crystal-on-silicon spatial light modulator from Meadowlark Optics 1920x1152 XY Phase Series, and were imaged onto the CMOS detector by using two confocal converging lenses (see Fig. 2), so that both the image and the  $SD$  are scaled by a factor of  $-f_2/f_1$ .

Figure 3 shows the measured interferograms for test wavefronts resulting from writing on the SLM spherical lenses of focal lengths  $f_s = 400, 500,$  and  $600$  mm. The  $\Lambda$ -plate spacing was  $\zeta = 12.0$  mm, producing a shear of  $SD \approx 2.4 \mu\text{m}$  over a beam waist  $w = 1.5$  mm. For  $\psi = 0$  and  $\psi = \pi/2$  the intensity approximately corresponds to that of the input beam and its  $x$ -derivative, respectively. As expected, the latter decreases by increasing  $f_s$  while the former remains fairly constant.

Figure 4 shows interferograms for the SLM displaying a cylindrical lens of focal length  $f_c = 400$  mm, whose axis is rotated



**Fig. 3.** Linear shearing interferograms of light focused by lenses implemented holographically via a SLM. In each row, from the top down,  $f_s = 400$  mm, 500 mm and 600 mm. The first and third columns contain respectively the experimental and theoretical profiles for  $\psi = 0$ , while the second and fourth columns show the same for  $\psi = 90^\circ$ . The plates' separation is  $\zeta = 12.0$  mm.



**Fig. 4.** Linear shearing interferograms for light focused by a cylindrical lens of focal length  $f_C = 400$  mm with different orientations, implemented on a SLM. The rows correspond to angles  $\gamma = 0^\circ$ ,  $30^\circ$ , and  $60^\circ$  between the lens axis and the shearing direction  $x$ . The first and third rows show the experimental and theoretical profiles for  $\psi = 0^\circ$ , while the second and fourth rows show the same for  $\psi = 90^\circ$ . The plates' separation is  $\zeta = 12.0$  mm.

with respect to the  $x$ -direction by  $0^\circ$ ,  $30^\circ$ , and  $60^\circ$ . The input's round shape is preserved for  $\psi = 0$  but not for  $\psi = \pi/2$ , since the square of the derivative gives two lobes that rotate and become fainter as the lens' focusing direction becomes orthogonal to the derivative direction.

A final example, shown in Fig. 5, corresponds to the measurement of the helicoidal wavefront of a hypergeometric-Gaussian beam [27] resulting from the passage of a Gaussian beam through a  $q$ -plate [23] (a SVAP whose optic axis distribution has a topological charge  $q$ , equal to unity in this case). The phase of this wavefront is  $\Phi(x, y) = \phi = \arctan(x, y)$ , the azimuthal angle. Again,  $\psi = 0$  essentially yields the input Gaussian intensity, while the pattern for  $\psi = \pi/2$  is dominated by the regions near the origin, where the phase's  $x$ -derivative is strongest. As mentioned earlier, the symmetry of this signal can be broken by slightly shifting  $\psi$  away from DM operation, allowing the deter-

mination of the sign of the derivative and hence the handedness of the vortex.

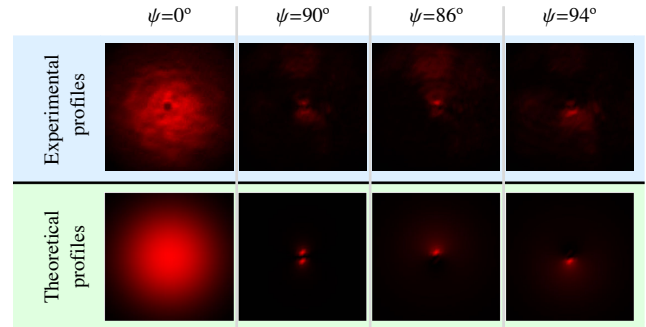


**Fig. 5.** Linear shearing interferograms (with  $\zeta = 20$  mm) for a beam emerging from a  $q$ -plate ( $q = 1$ ). The top row shows the measured profiles and the bottom row shows the theoretical predictions. From left to right, the columns correspond to  $\psi = 0^\circ$ ,  $90^\circ$ ,  $86^\circ$  and  $94^\circ$ , respectively. Note that the sign of the  $x$ -derivative can be inferred from either of the latter two.

*Extension to radial and other geometries* – An important feature of SVAP-based shearing is the freedom it provides for implementing different geometries, as discussed in the Supplement 1. This is now illustrated by replacing the  $\Lambda$ -plates with two Geometric Phase Lenses (GPLs), so that the interferometer performs a radial shear, resulting from the interference of two differently sized replicas of the test beam (Fig. 6). In this case, instead of a SD parameter we have a shear expansion (SE) between the replicas. A GPL acts as a positive or negative lens depending on the circularly polarized input handedness [28]. The SE is

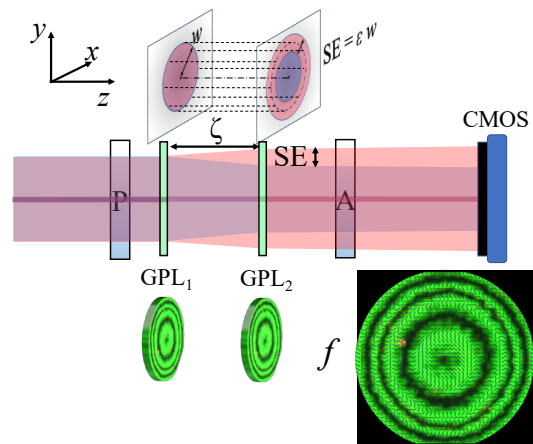


**Fig. 6.** Sketch of a radial GPSI. This device is identical to the GPSI in Fig. (1), but with the  $\Lambda$ -plates replaced by GPLs with focal length  $f = (130 \pm 1)$  mm. The bottom-right inset shows the fast-axis distribution of the GPLs we fabricated, superimposed onto the experimental polarization fringe pattern of the GPL.

proportional to the distance  $\zeta$  between the GPLs. The resulting interferometer is essentially equivalent to the one introduced by Hariharan [29], but using GPLs allows a much simpler set-up. When  $\zeta$  is much smaller than the focal length  $f$  of the GPLs,  $SE \approx \zeta w / f$  where  $w$  is the input beam spot size, and the third term in Eq. (3),  $\text{Im}(SD^*)$ , returns the beam's radial derivative. This is shown in Fig. 7 for a cylindrical lens of focal length

$f = (400 \pm 1)$  mm. Details of the method will be provided in a upcoming work.

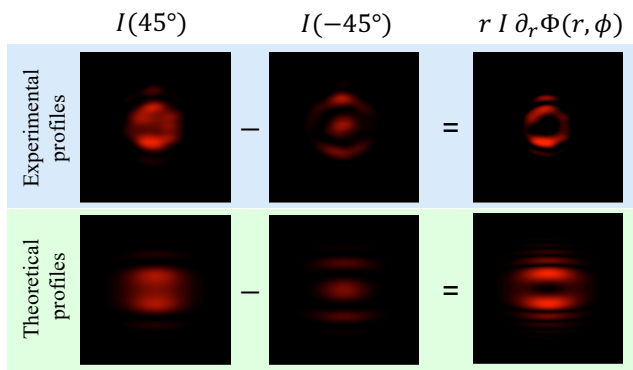


**Fig. 7.** Radial shearing interferogram of a cylindrical lens phase profile with focal length  $f = (400 \pm 1)$  mm. The derivative pattern can be obtained as difference between the interference pattern at  $\psi = +45^\circ$  and  $\psi = -45^\circ$ ,  $\psi$  being the mismatch angle between the input polarization direction and the axis of the analyzer A. On the upper line, we show a numerical simulation of the derivative pattern; on the lower line, we show the experimentally observed pattern.

## 1. CONCLUDING REMARKS

We have shown that shearing interferometry can be implemented efficiently using a pair of geometrical phase optical elements, such as SVAPs. This approach enhances the flexibility of this type of interferometer in terms of reusability, manageability, compactness and independent control of the two fundamental parameters: SD/SE and SP. More importantly, it is suitable not only for linear shearing but also other geometries such as radial shearing. The spatial parameters SD/SE, in fact, are related to the geometric properties of SVAPs, while SP is related to suitable polarization manipulations. The full potential of the approach, however, is clear when the SVAPs are tailored to achieve non-uniform derivatives, which would be difficult if not unfeasible by other setups.

Also notice that, while SVAPs can be implemented with other technologies such as dielectric metasurfaces, the use of liquid crystals not only guarantees a high transmissivity but also allows fine-tuning of the operation wavelength and control of the overall shearing efficiency by means of an externally applied voltage. In particular, the possibility to switch the device on and off enables combining, upon requirement, the action of several shearing mechanisms allowing not only differentiation with respect to a single variable, but in general a full 2D differential.

## FUNDING INFORMATION

This work was supported by the University Research Funding Program (DR n. 3425-10062015); the European Research Council (ERC), under grant no. 694683 (PHOSPhOR); National Science Foundation (NSF) (PHY-1507278); the University of Rochester Pump Primer II Award (OP212647), CONACYT fellowship awarded to L.A.C., and M.A.A. acknowledges support from the Excellence Initiative of Aix-Marseille University-A\*MIDEX, a French “Investissements d’Avenir” programme.

## ACKNOWLEDGMENTS

M.A.A. thanks Jim Zavislan for useful discussions.

See [Supplement 1](#) for supporting content.

## REFERENCES

1. D. Malacara, *Optical Shop Testing*, Wiley Series in Pure and Applied Optics (Wiley, 2007).
2. B. Piccirillo, S. Slussarenko, L. Marrucci, and E. Santamato, *Nat. Comm.* **6**, 8606 (2015).
3. W. J. Bates, *Proc. Phys. Soc.* **59**, 940 (1947).
4. M. V. R. K. Murty, *Appl. Opt.* **9**, 1146 (1970).
5. Y. Y. Hung, *Opt. Commun.* **11**, 132 (1974).
6. J. C. Wyant, *Appl. Opt.* **12**, 2057 (1973).
7. R. P. S. M. V. R. K. Murty, *Opt. Eng.* **19**, 19 (1980).
8. H.-H. Lee, J.-H. You, and S.-H. Park, *Opt. Lett.* **28**, 2243 (2003).
9. D. W. Griffin, *Opt. Lett.* **26**, 140 (2001).
10. M. P. Kothiyal and C. Delisle, *Appl. Opt.* **24**, 4439 (1985).
11. L. Wang, L. Liu, Z. Luan, J. Sun, and Y. Zhou, *Optik - Int. J. for Light. Electron Opt.* **124**, 1215 (2013).
12. L. Gu, L. Liu, and e. a. S. Hu, *Opt. Rev.* (2017).
13. S. Debrus, *Opt. Commun.* **20**, 257 (1977).
14. C. v. K. W. J. C. Falldorf, S. Osten, *Opt. Lett.* **34**, 2727 (2009).
15. P. Bon, G. Maucort, B. Wattellier, and S. Monneret, *Opt. Express* **17**, 13080 (2009).
16. T. Ling, Y. Yang, X. Yue, D. Liu, Y. Ma, J. Bai, and K. Wang, *Appl. Opt.* **53**, 7144 (2014).
17. T. Ling, Y. Yang, D. Liu, X. Yue, J. Jiang, J. Bai, and Y. Shen, *Appl. Opt.* **54**, 8913 (2015).
18. S. Velghe, J. Primot, N. Guérineau, R. Haidar, S. Demoustier, M. Cohen, and B. Wattellier, *Proc. SPIE* **6292**, 6292 (2006).
19. S. Pancharatnam, *Proc. Indian Acad. Sci. Sect. A* **44**, 247 (1956).
20. G. C. T. Malhorta, *Phys. Rev. Lett.* **120**, 233602 (2018).
21. M. Berry, *J. Mod. Opt.* **34**, 1401 (1987).
22. L. Marrucci, C. Manzo, and D. Paparo, *Phys. Rev. Lett.* **96**, 163905 (2006).
23. B. Piccirillo, V. D’Ambrosio, S. Slussarenko, L. Marrucci, and E. Santamato, *Appl. Phys. Lett.* **97**, 241104 (2010).
24. F. Zernike, *Physica* **9**, 686 (1942).
25. F. Zernike, *Physica* **9**, 974 (1942).
26. P. B. Dixon, D. J. Starling, A. N. Jordan, and J. C. Howell, *Phys. Rev. Lett.* **102**, 173601 (2009).
27. E. Karimi, G. Zito, B. Piccirillo, L. Marrucci, and E. Santamato, *Opt. Lett.* **32**, 3053 (2007).
28. B. Piccirillo, M. F. Picardi, L. Marrucci, and E. Santamato, *Eur. J. Phys.* **38**, 034007 (2017).
29. P. Hariharan and D. Sen, *J. Sci. Instrum.* **38**, 428 (1961).